Relationships between Tropical Cyclone Intensity and Eyewall Structure as Determined by Radial Profiles of Inner-Core Infrared Brightness Temperature

ELIZABETH R. SANABIA AND BRADFORD S. BARRETT

Oceanography Department, U.S. Naval Academy, Annapolis, Maryland

CAITLIN M. FINE

Department of Atmospheric Science, Colorado State University, Fort Collins, Colorado

(Manuscript received 28 October 2013, in final form 29 July 2014)

ABSTRACT

Radial profiles of infrared brightness temperature for 2405 different satellite observations from 14 western North Pacific tropical cyclones (TCs) from the 2012 season were analyzed and compared to intensity and changes in intensity. Four critical points along the inner core of each infrared (IR) brightness temperature (BT) profile were identified: coldest cloud top (CCT), first overshooting top (FOT), and lower (L45) and upper (U45) extent of the inner eyewall. Radial movement of the mean CCT point outward with increasing TC intensity, combined with subsequent warming of the mean L45 point with intensity, highlighted structure changes that are consistent with eye and eyewall development. When stratified by latitude and vertical wind shear, the CCT point moved radially outward for all cases, notably at higher intensities for lower-latitude TCs and at lower intensities for higher-latitude TCs. The majority of the warming of the L45 point with increasing intensity occurred for low-latitude and low-shear cases. Slopes of IR BT between the four critical points were statistically significantly negatively correlated with intensity, indicating that stronger (weaker) TCs had more (less) negative slopes of IR BT and more (less) vertical eyewall profiles. Furthermore, except in high-shear cases, the most negative correlations were found in the inner eyewall, consistent with results from recent studies based on radar reconnaissance data. Finally, 12-h changes in slope were found to lead 12-h changes in intensity most often at higher latitudes, providing evidence that changes in the secondary TC circulation may lead changes in the primary TC circulation for both strengthening and weakening TCs.

1. Introduction

Observations of the inner portion of tropical cyclones (TCs) have long been considered important, particularly to determine TC intensity. So much so that despite the associated risk, routine aircraft reconnaissance programs were begun in the 1940s (Markus et al. 1987) to determine the TC center location and to measure central pressure, maximum wind speed, and direction of motion, as those were among the critical data needed for TC warning systems. With the launch of polar-orbiting weather satellites in the 1960s, and then geostationary weather satellites later in the 1960s and 1970s, remotely sensed observations of TC cloud features became routinely available (Sheets 1990). Techniques quickly followed to capitalize on these new satellite observations and to associate them with wind and pressure measurements of TC strength (e.g., Fett 1964; Sadler 1964; Fritz et al. 1966; Erickson 1967). One of the most important and commonly used techniques, and one that is still widely used today, was developed by Dvorak (1972; 1975), who recognized that kinematic organizational patterns of TC clouds could be used to reliably and systematically estimate the current TC intensity (Velden et al. 2006). One of the most important updates to this methodology was to include infrared (IR) brightness temperatures (Dvorak 1984, 1995), which added an important thermodynamic component to the original kinematic one. This technique for estimating TC intensity based on remote sensing measurements, known now as the Dvorak technique, proved transformational for the operational TC community, as it allowed all TCs remotely sensed by satellites to be

Corresponding author address: Bradford S. Barrett, 572C Holloway Rd., Annapolis, MD 21402.
E-mail: bbarrett@usna.edu

DOI: 10.1175/MWR-D-13-00336.1

assigned a current intensity, including those in basins without aircraft reconnaissance and those located far from land. It remains a reasonably accurate tool today, with as many as 50% of the Dvorak-based maximum wind speed estimates coming within 5 kt (1 kt = 0.51 m s^{-1}) of the best-track values based on reconnaissance aircraft measurements (Brown and Franklin 2004). Despite this success, however, geostationary satellite measurements of the TC inner core are not fully used by current intensity estimation techniques, a gap that this study will address.

One of the reasons for the success of the Dvorak technique is that the IR brightness temperatures (BTs) used to assign current intensity are themselves indicators of important structural properties of the inner portion of the TC. As an example, cloud-top temperature roughly represents cloud-top height, as colder clouds are located higher in the atmosphere [this temperature–height relationship varies as a function of latitude and time of year, since tropopause heights are lower toward the poles and during the winter season; Thuburn and Craig (1997); Kossin and Velden (2004); Raman and Chen (2014)]. The temperature (height) of the clouds in the central region of a TC indicates the intensity of the updraft, which is one component of the secondary circulation (Eliassen 1951; Willoughby 1979; Shapiro and Willoughby 1982). Colder (taller) clouds are associated with more vigorous updrafts, which would be related to a more intense secondary circulation pattern. Shapiro and Willoughby (1982) related the intensity of the secondary circulation to maximum tangential surface winds. The Dvorak technique also examines the difference in temperature between the warmest BT in the eye and the coldest BT in the eyewall cloud (Velden et al. 1998); however, it does not consider the radial distance between points, which this study will explore. Greater temperature differences between the eye and eyewall mean that updrafts in the TC core are stronger, and current Dvorak-type techniques relate greater brightness temperature differences to more intense surface winds.

Besides cloud top and differences in BTs measured by satellites, other parameters specific to the TC core environment also have been studied. Notably, several recent studies (e.g., Corbosiero et al. 2005; Schubert and McNoldy 2010; Hazelton and Hart 2013) have addressed the slope of the eyewall cloud as estimated by aircraft-based radar reflectivities. Similar to satellite brightness temperature measurements, the slope of these reflectivity surfaces is another important indicator of TC structure that can be empirically related to TC intensity. For an idealized, axisymmetric vortex in gradient wind balance, the secondary circulation resulting from a heat source (such as eyewall convection) must slope outward with height to satisfy the thermal wind balance for a warm-core vortex (Shapiro and Willoughby 1982). The more vertical this slope, the more intense the TC, which is a property that has been noted in both observations (Black et al. 1994; Corbosiero et al. 2005) and model output (Ritchie and Frank 2007; Zhao et al. 2012). Other studies of eyewall slope (Shea and Gray 1973; Stern and Nolan 2009; Rogers et al. 2012) have focused on changes in positions of the radius of maximum wind (RMW) with height. While results from these studies were generally inconclusive, studies of eyewall slope that focused on the slope of radar reflectivity surfaces consistently found that more intense TCs were characterized by more vertical outward-sloping reflectivity surfaces in the inner core (Jorgensen 1984; Marks 1985; Corbosiero et al. 2005; Schubert and McNoldy 2010; Hazelton and Hart 2013). The present study builds on these findings by calculating slope based on IR BTs in the inner core, as measured by a geostationary satellite. Because these observations are much more frequent than those for radar reflectivity, particularly in basins such as the western North Pacific that do not have routine aircraft reconnaissance, the findings of this study could serve to enhance operational intensity estimation techniques.

Despite the advances in observational radar and satellite techniques, physical structures of the TC inner core, such as cloud height and slope, remain relatively understudied. Furthermore, current Dvorak-based techniques that estimate TC intensity using differences in inner-core BTs primarily focus on the brightness temperature at two points: the warmest (normally in the eye) and the coldest (normally in the eyewall) (Olander and Velden 2007). Radar observations have shown significant variability in slope within the inner core, particularly in the slope of radar reflectivity surfaces, suggesting that it may be possible to use differences in cloud-top temperatures at more than just two points in the TC inner core to estimate current intensity (Piñeros et al. 2011; Ritchie et al. 2012). This study aims to partially fill both of those gaps by using IR BTs from geostationary satellite observations to calculate the cloud-top slope at multiple points in the inner core of western North Pacific TCs and to relate those slope measurements to TC intensity. Section 2 contains a detailed description of the methodology used to calculate and analyze critical points along the IR BT profiles. Results are presented in section 3. Conclusions and implications of the results are discussed in section 4.

2. Data and methodology

a. Data

A total of 2405 unique geostationary satellite observations (Fig. 1) made during the lifetimes of 14 western

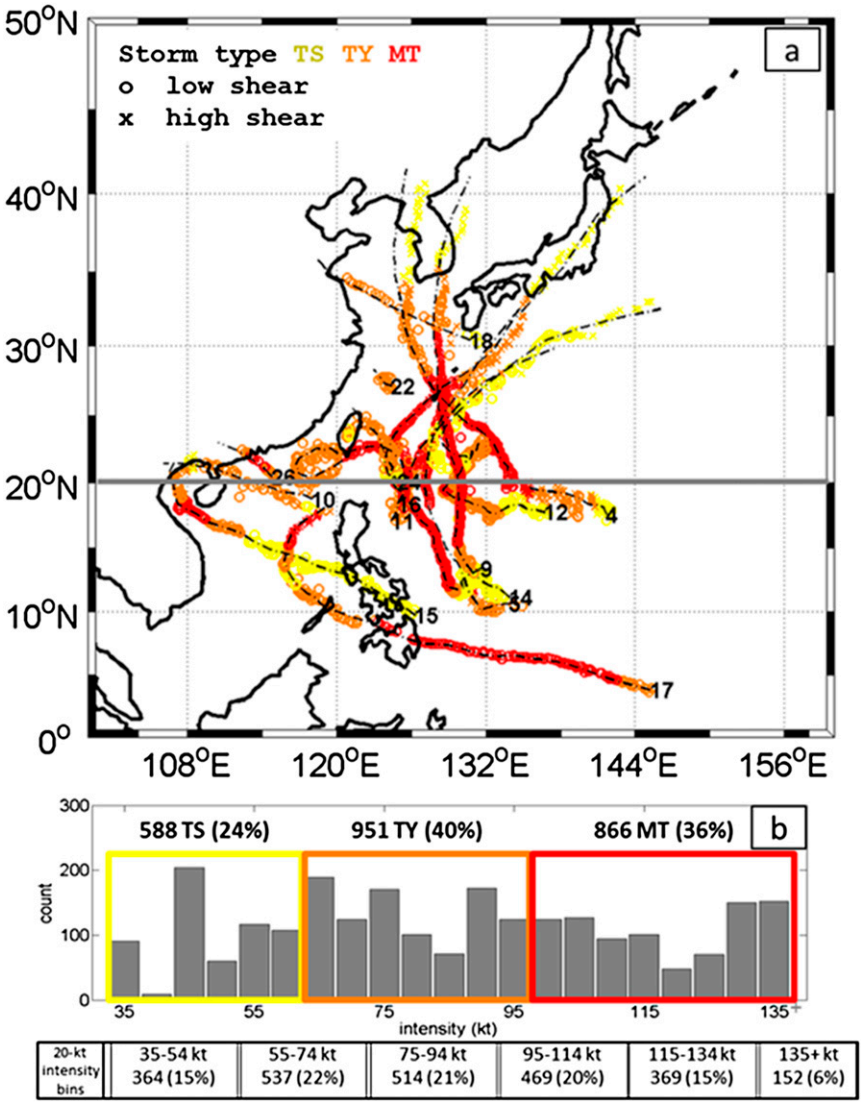

FIG. 1. Locations and intensities of TCs included in this analysis. (a) TC centers manually identified from satellite imagery are marked with an open circle (○) symbol for cases of 850–200-hPa vertical wind shear $\leq 10\,m\,s^{-1}$ and a crisscross (×) for wind shear $>10\,m\,s^{-1}$. Coded intensities are yellow for tropical storm (TS, 34–63 kt); orange for typhoon (TY, 64–99 kt), and red for major typhoon (MT, 100+ kt). Dotted–dashed black lines indicate the JTWC best-track location over the period of the available satellite data. The gray line at 20°N separates the northern and southern latitude cases. (b) Counts of profiles in different intensity categories include 5-kt increments (gray bars), 20-kt increments (boxed numbers across bottom), and TS, TY, and MT categories (numbers across top).

North Pacific TCs that reached at least typhoon (64 kt) intensity in during 2012 season were examined for this study (Table 1). Ten of the typhoons exceeded 100-kt intensity, and available observations for all but two extended beyond 1 day. Infrared (IR; channel 1, 10.8 μm) and water vapor (WV; channel 3, 6.8 μm) satellite data used in this study came from the *Multifunctional Transport Satellite-2* (*MTSAT-2*), a geostationary satellite operated by the Japan Meteorological Agency (JMA). Each of the 2405 satellite observations were available approximately every 30 min on a 4-km grid and were provided by the Marine Meteorology Division at the Naval Research Laboratory (NRL), Monterey, California. Tropical cyclone intensities, defined by maximum surface winds, were taken from the Joint Typhoon Warning Center (JTWC) best-track product (Chu et al.

TABLE 1. List of typhoons included in this study, ordered by JTWC best-track number. Start–stop dates and times and counts of satellite observations for TS, TY, and MT intensities, along with total observations, are given. Typhoon number is also indicated in Fig. 1. All observations in 2012.

Typhoon	Name	First obs	Final obs	No. of TS (34–63 kt)	No. of TY (64–99 kt)	No. of MT (100+ kt)	Total No. of obs
4	Mawar	0832 UTC 2 Jun	1132 UTC 5 Jun	4	44	11	59
5	Guchol	0632 UTC 14 Jun	2232 UTC 18 Jun	0	47	34	81
9	Vicente	0632 UTC 23 Jul	2332 UTC 23 Jul	0	10	6	16
10	Saola	0632 UTC 30 Jul	0532 UTC 2 Aug	24	48	0	72
11	Damrey	0632 UTC 1 Aug	1132 UTC 2 Aug	3	27	0	30
12	Haikui	1832 UTC 6 Aug	0532 UTC 7 Aug	0	12	0	12
14	Kai-tak	1832 UTC 15 Aug	1132 UTC 17 Aug	6	36	0	42
15	Tembin	0632 UTC 20 Aug	1032 UTC 27 Aug	0	114	50	164
16	Bolaven	0732 UTC 20 Aug	1101 UTC 28 Aug	68	107	136	311
17	Sanba	0632 UTC 11 Sep	1001 UTC 17 Sep	66	53	165	284
18	Jelawat	1932 UTC 20 Sep	1732 UTC 30 Sep	118	59	293	470
22	Prapiroon	1532 UTC 7 Oct	0030 UTC 19 Oct	161	267	34	462
24	Son-tinh	0030 UTC 24 Oct	2313 UTC 28 Oct	126	57	34	217
26	Bopha	0630 UTC 30 Nov	1030 UTC 8 Dec	12	70	103	185
			Total	588	951	866	2405

2002) at 6-h increments. Of the 2405 satellite BT observations, 588 (24.4%) were made in TCs of tropical storm intensities (34–63 kt, labeled TS hereafter), 951 (39.6%) were made in TCs with typhoon intensities less than 100 kt (i.e., 64–99 kt, labeled TY hereafter), and 866 (36.0%) were made in TCs of major typhoon intensities at or above 100 kt, (i.e., 100+ kt, labeled MT hereafter). Given the lack of routine aircraft reconnaissance during the 2012 western North Pacific season, it is likely that the majority of these best-track intensities were at least partially based on Dvorak intensity estimates.

b. Methods

1) Radial profile construction

Radial profiles of IR BTs formed the basis for this study and required the identification of the TC center location for each satellite observation. Nonlinear TC motion between the available JTWC analysis times (0000, 0600, 1200, and 1800 UTC) precluded the use of TC center locations determined by interpolation of the JTWC best track. Instead, latitude and longitude coordinates of the TC centers were visually (manually) identified in every satellite observation to a single BT pixel, yielding a precision that approximately matched the *MTSAT-2* horizontal (4 km) resolution. Although manual center identification was used for this study, other center-identification techniques, including automated methods (e.g., Wimmers and Velden 2010), potentially could be employed to create the radial profiles used in this study.

The IR BT radial profiles were constructed by storm centering the digital data, converting the Cartesian latitude and longitude gridded data into a polar coordinate system (with radius r and azimuth θ), and azimuthally averaging satellite IR and WV BTs at 1.0° θ intervals every 2 km from the TC center, similar to the methodology of Bankert and Tag (2002). Because of the choices of the r and θ intervals, the outer part of the TC (beyond about 200 km from the center) was undersampled relative to the inner part. However, the majority of the critical points (defined below) were located inside 100 km from the TC center, and this region was well sampled by the chosen r and θ spacing. Furthermore, results of this study were found to not be sensitive to variations in the choice of spacing of either r (examined every kilometer, from 2 to 4 km) or θ (examined every degree, from 1° to 4°).

To begin investigating the relationship between inner-core cloud-top structure and TC intensity, several mean radial profiles were constructed. First, the 2405 individual IR BT profiles (Fig. 2a, gray lines) were averaged, resulting in a mean IR BT radial profile (Fig. 2a, black line) representing TCs of all intensities. The individual profiles were then stratified by intensity, based on the JTWC best-track intensity closest in time to the satellite observation (Fig. 1b). Mean radial profiles were constructed (Figs. 2b–d, black lines) by averaging the member profiles (Figs. 2b–d, gray lines) in each of these three intensity subcategories. One standard deviation above and below each mean was plotted to illustrate the variability in the profiles (Fig. 2, dashed black lines).

2) Critical point identification

Four critical points were identified within 200 km from the TC center in each radial profile of IR BT and were selected based on physical significance [the innermost 200 km was selected as the focus area after Maclay et al. (2008), who defined the TC core as the

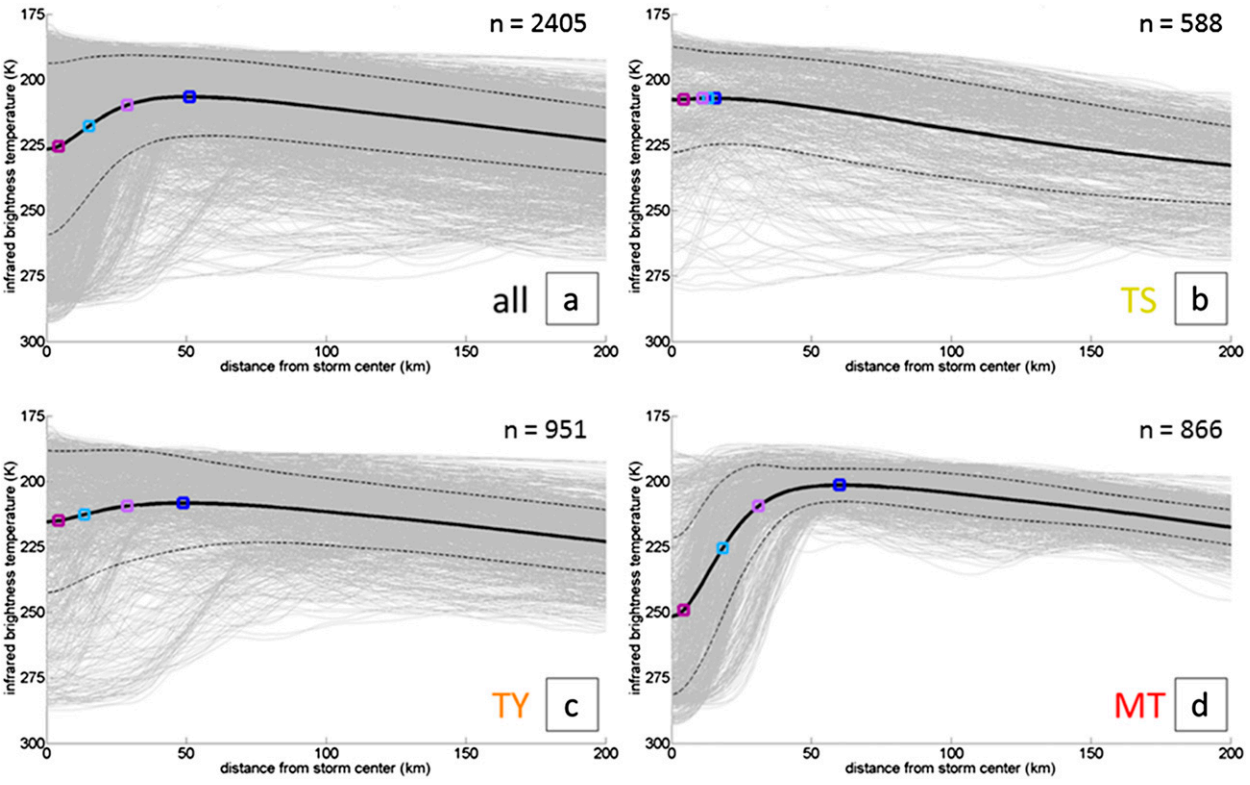

FIG. 2. Infrared BT profiles (gray lines) for (a) all TCs, and only TCs with (b) TS, (c) TY, and (d) MT intensities. Critical points for CCT, FOT, and L45 and U45 are represented by dark blue, light blue, magenta, and light purple squares, respectively. Mean (black lines) and standard deviation (dashed black lines) for each intensity category are also plotted. Number of profiles in each category is indicated in the header in each panel.

region within 200 km of the TC center]. Critical point 1 was the radial location of the coldest cloud top (CCT). The CCT was identified as the minimum IR BT in the inner 200 km of the TC. Critical point 2, the radial location of the first overshooting top (denoted FOT hereafter), was identified using WV-IR BT differences following Fritz and Laszlo (1993) and Olander and Velden (2009). The FOT was determined by locating the radial point closest to the TC center (i.e., the minimum radial distance) where a positive WV–IR BT difference (i.e., convection that penetrated the tropopause) was present at any azimuth. To facilitate analysis with the other three critical points (which were all based on IR BT), and since the magnitude of overshooting tops was not a primary focus here, the FOT was assigned the BT at the FOT radial location within each IR profile (as opposed to assigning it the WV or WV–IR BT at that radial point).

The third and fourth critical points were selected to define a lower and upper extent of the inner eyewall, respectively. The lower extent (L45) was identified as the first 45° upturn inflection point, which is where the orientation of the IR profile changed from horizontal to vertical. The upper extent (U45) was identified as the first 45° downturn inflection point radially outward from L45, which is where the orientation of the IR profile changed from vertical to horizontal. The choice of 45° as inflection points follows from the many observational studies that note the slope of the eyewall often exceeds 45° (Hawkins and Imbembo 1976; Marks 1985; Black et al. 1994; Corbosiero et al. 2005; Hazelton and Hart 2013). These two critical points were located in two steps. First, the components of each IR radial profile were nondimensionalized to create a nondimensional profile. The nondimensional IR BTs (NBT_i) were calculated as

$$NBT_i = \frac{BT_{max} - BT_i}{BT_{max} - BT_{CCT}}, \quad (1)$$

where BT_{max} is the warmest brightness temperature in the innermost 100 km, BT_i is the brightness temperature at radial point i, and BT_{CCT} is the brightness temperature at critical point CCT. The nondimensional radial distances (Nr_i) were calculated as follows:

$$\mathrm{Nr}_i = \frac{r_{\max} - r_i}{r_{\max} - r_{\mathrm{CCT}}}, \tag{2}$$

where $r_{\max}$ is the radial distance from the TC center to the warmest brightness temperature in the innermost 15 km, r_i is the radial distance from the TC center to the radial point i, and r_{CCT} is the radial distance from the TC center to the critical point CCT. The 15-km threshold was based on eye size as defined in Shapiro and Willoughby (1982). By nondimensionalizing, the brightness temperature at each CCT was assigned the value of one, and the radial distance at each CCT was also assigned the value of one. Second, profile angles (α_i) were calculated at every radius r as

$$\alpha_i = \arctan\left(\frac{\mathrm{NBT}_{i+1} - \mathrm{NBT}_{i-1}}{\mathrm{Nr}_{i+1} - \mathrm{Nr}_{i-1}}\right), \tag{3}$$

where NBT_{i+1} (NBT_{i-1}) is the nondimensional brightness temperature one radial increment ahead of (behind) the radial point i at the nondimensional radial distance Nr_i. Critical point L45 was designated as the radial location closest to the TC center where α_i first exceeded 45°, and critical point U45 was designated as the first point after L45 where α_i was less than 45°.

This procedure for identifying the L45 and U45 critical points required that CCTs not be located exactly at the TC center. Of the 2405 profiles examined, CCT was located at the TC center [possibly indicative of central dense overcast (CDO) conditions] in 394 cases, thereby reducing the profiles available for L45 and U45 identification by 16.5%. Critical point 2 (FOT; overshooting top closest to TC center) was located in the inner core (defined as the region from 0 to 200 km radially outward from the TC center) in 2363 (99.5%) of the profiles. Critical points 3 (L45) and 4 (U45) were identified less often [in 1708 and 1707 (71.0%) of the profiles, respectively]: they did not exist in the 394 profiles when the CCT was located at the storm center, and they also did not exist in weaker TCs where the radial profile was not sufficiently sloped to register a 45° angle (i.e., did not exhibit an eye or eyewall structure). Stratifying by intensity confirmed that the L45 and U45 critical points were identified more often in strong TCs, occurring in 96.7% of the profiles observed during TC intensities greater than or equal to 100 kt, compared to 64.1% of the profiles collected when TC intensities were between 64 and 99 kt and 44.4% of profiles observed when intensities were less than 64 kt. For most profiles, the critical points were located in the following order (radially outward from the TC center): L45, FOT, U45, and CCT.

Critical points were calculated for both mean and individual IR BT profiles. To evaluate changes in mean cloud-top structure with intensity, critical points CCT, L45, and U45 were determined by applying the steps listed above to the four mean IR BT radial profiles (Fig. 2). Radial distances of critical point FOT for the four mean profiles were calculated by averaging the FOT radial distances in all the member profiles in each category. The IR BT at that radius in the mean profile was then assigned as the FOT BT in the respective intensity subcategory.

To facilitate further investigation of the structural features represented by the four critical points, the IR BT profiles were subdivided into six 20-kt intensity bins (Fig. 1b). Mean critical points were calculated for each bin by averaging the radial distance and IR BT of each critical point from the hundreds of profiles within that bin. As previously discussed, critical points could not be identified in all profiles. Thus, mean critical point values were calculated for two subsets of profiles. The first subset was constrained to profiles in which all four critical points were present, thereby focusing the analysis on the 1688 (70.2%) of profiles with all four critical points present. The second subset included every available critical point, which totaled 2405 CCTs, 1708 L45s, 1707 U45s, and 2363 FOTs. Mean critical points were calculated by averaging the radial distance and IR BT of the member profiles in each of the six intensity bins and were used to examine how structural features evolved with intensity. Results are explored in section 3.

3) Inner-core cloud-top slopes

The structure of inner-core convection was quantitatively examined through six slopes of IR brightness temperature between the four critical points defined above (Fig. 3). Slopes were calculated by dividing the change in IR BT between two critical points by the radial distance between those two critical points. For example, the L45–FOT lower eyewall slope, $S_{\mathrm{L45\text{-}FOT}}$, represented the departure from horizontal of the IR BT profile of the lower eyewall and was calculated as follows:

$$S_{\mathrm{L45\text{-}FOT}} = \frac{\mathrm{BT}_{\mathrm{L45}} - \mathrm{BT}_{\mathrm{FOT}}}{r_{\mathrm{L45}} - r_{\mathrm{FOT}}}, \tag{4}$$

where $\mathrm{BT}_{\mathrm{L45}}$ represents the IR brightness temperature at the lower 45° critical point L45, $\mathrm{BT}_{\mathrm{FOT}}$ represents the IR brightness temperature at the first overshooting top critical point FOT, and r_{L45} and r_{FOT} represent the radial distances of the L45 and FOT critical points, respectively, from the TC center. A negative slope indicated that IR BT decreased radially outward between the two critical points. A more negative slope indicated a more vertical profile of IR BT. Together, the lower (L45–FOT) and middle (FOT–U45) eyewall

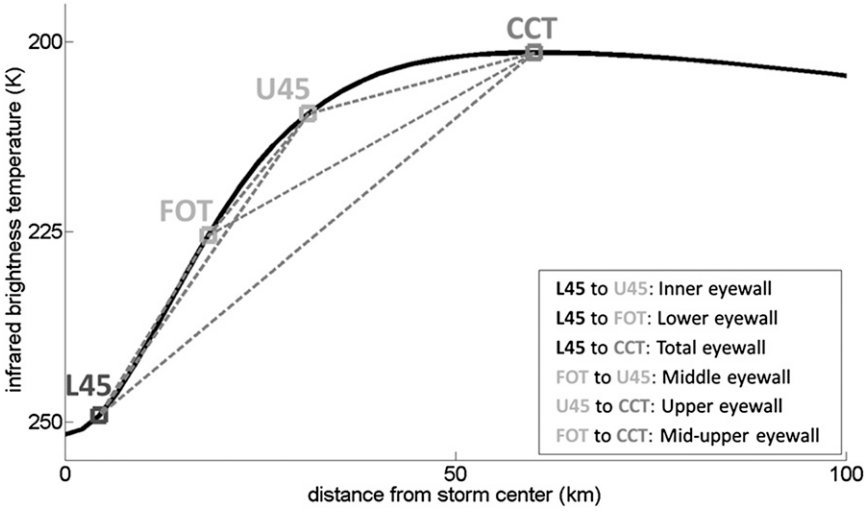

FIG. 3. Slope segments identification and naming convention, here for the MT mean profile.

sections composed the inner eyewall (L45–U45). It was noted that on rare occasions (typically in weakest profiles), the FOT was not located between L45 and U45, and therefore the physical relationships associated with this naming convention were not applicable to every profile. The U45–CCT segment physically represented the upper eyewall, and the L45–CCT section composed the total eyewall for the purpose of this study. The final segment, FOT–CCT, outlined the mid- to upper portion of the TC inner core and spanned both the middle eyewall (FOT–U45) and the upper eyewall (U45–CCT) segments. Although both WV and IR BTs were used to determine the location of the FOT, slopes that used the FOT critical point were calculated using IR BTs at the FOT point. Thus, the methodology for each slope calculation followed Eq. (4), and all slopes reflected radial changes in IR BT between the six critical points. This methodology for calculating slope (i.e., using the azimuthal inner-core cloud-top brightness temperatures) parallels similar definitions for other eyewall surfaces in previous studies (e.g., Hazelton and Hart 2013).

Because critical points were not able to be identified for all profiles (most frequently when the coldest clouds were located at the storm center, or when weak TCs had flat IR BT profiles that did not incline more than 45° when nondimensionalized), and because critical points were sometimes collocated with each other or were located beyond 200 km from the TC center, some slopes were undefined. Availability of each slope for each intensity category is listed in Table 2. Weaker storms generally had fewer slopes defined, while stronger storms generally had more slopes defined. Stronger TCs more often had defined slopes because (a) their critical points existed and (b) their critical points were not collocated or were not located within the TC inner core. For all slopes, Pearson product-moment linear correlation coefficients were calculated to quantify relationships between slope and intensity.

To examine *changes* in slope with corresponding *changes* in TC intensity, IR BT profiles were time averaged to synoptic times 0000, 0600, 1200, and 1800 UTC to match the temporal resolution of the surface wind data available from JTWC. To maximize the representativeness of the JTWC best-track data, all slopes within 1.5 h of a synoptic time were included in the averages, and changes in those averaged values were compared with changes in TC intensity. This 3-h window, which is narrower than the 6-h window, allowed for the

TABLE 2. Number and percentage of slopes for each intensity category. Percentages calculated as fraction of total number of slopes available for a respective intensity category [e.g., the L45–U45 slope existed in 260 of the 588 TS profiles (44.2%)].

Intensity category (kt)	Total No. of profiles	L45–U45		L45–FOT		L45–CCT		FOT–U45		U45–CCT		FOT–CCT	
TS (34–63)	588	260	44.2%	224	38.1%	261	44.4%	241	41.0%	237	40.3%	396	67.3%
TY (64–99)	951	610	64.1%	578	60.8%	610	64.1%	601	63.2%	580	61.0%	776	81.6%
MT (≥100)	866	837	96.7%	820	94.7%	837	96.7%	811	93.6%	830	95.8%	850	98.2%

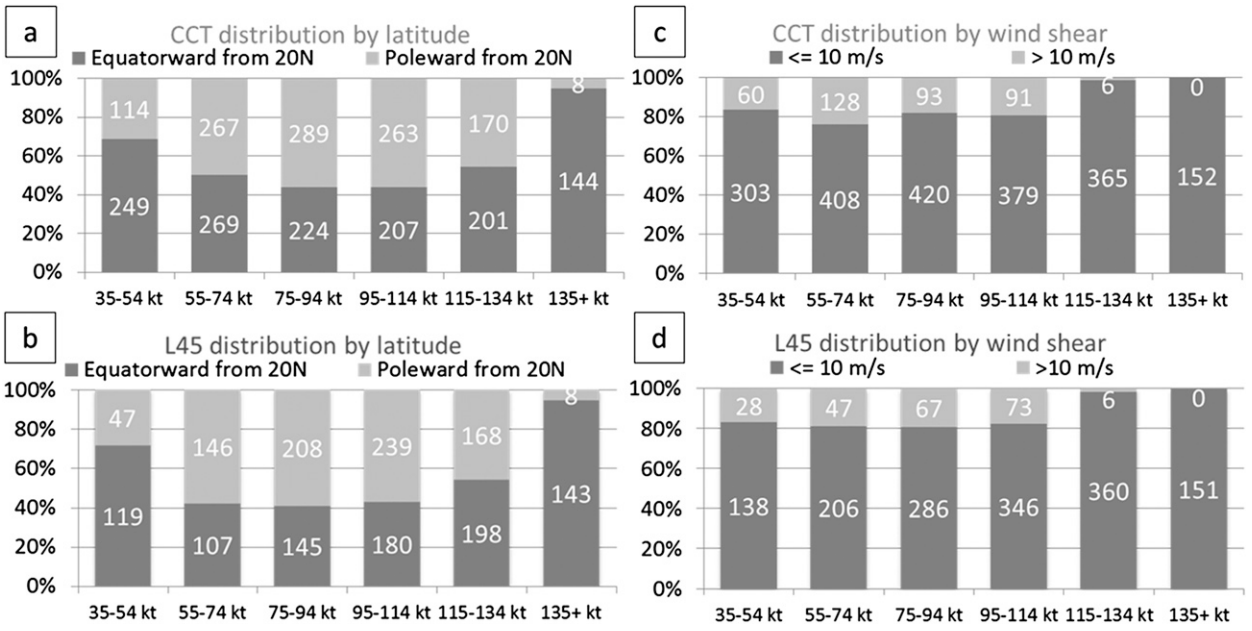

FIG. 4. Distribution of critical points (top) CCT and (bottom) L45 for six intensity subcategories, stratified by (a),(b) latitude and (c),(d) vertical wind shear.

straightforward comparison between current slope and current intensity and was used to try to better capture changes in slope with changes in intensity. The narrower time window resulted in fewer slope observations being available to compare to changes in intensity. As with comparisons between slope and intensity, Pearson product-moment linear correlation coefficients were calculated to quantify the relationship between 6-, 12-, and 24-h changes in slope and in intensity. Finally, 6- and 12-h changes in slope were compared to the following and preceding 6- and 12-h changes in intensity to investigate potential lead–lag relationships between structure and intensity. Only the 12- and 24-h results are reported here, as they showed the strongest relationship between slope and intensity.

4) STRATIFICATION BY LATITUDE AND VERTICAL WIND SHEAR

To further examine the evolution of the eyewall structure with intensity, the mean critical point and slope analyses were repeated for subgroups of higher and lower latitudes and of high and low vertical wind shear (Fig. 4). The median central latitude for the 2405 cases was located at 19.4°N; consequently, 20°N was chosen as a dividing line between the lower- and higher-latitude cases. The 10 m s^{-1} threshold for vertical wind shear was selected based on criteria presented in Corbosiero and Molinari (2002), who found significant asymmetries in vertical motion in cases where vertical wind shear exceeded 10 m s^{-1}. For the vertical wind shear classification, the primary shear predictor in the Statistical Hurricane Intensity Prediction Scheme (SHIPS) developmental dataset for the western North Pacific (M. DeMaria 2014, personal communication) was utilized to determine the vertical wind shear at each synoptic time. This SHIPS predictor (SHDC) provided a shear magnitude between 850 and 200 hPa as averaged from 0 to 500 km relative to the 850-hPa vortex center. While a predictor in the developmental dataset, the ''perfect prog'' values (i.e., the best-track positions and analysis fields) were used, rather than forecast positions and forecast fields (M. DeMaria 2014, personal communication), increasing the accuracy of the shear value.

3. Results

a. Mean IR BT profiles

In the mean radial profile of all 2405 IR BT observations (Fig. 2a), the IR BTs decreased from the storm center outward to the radius of the CCT critical point, then increased slowly from the CCT radius outward to the 200-km extent of the TC inner core (note that the *y* axis is inverted in Figs. 2, 3, 5, 8, and 9b). The point marking the lower extent of the inner eyewall (L45, magenta square in Fig. 2a) was the most radially inward and the warmest of the four critical points, located 4.45 km from the TC center in the mean radial profile

TABLE 3. Radial distance (r) from the TC center (in km) and IR BT (K) of each critical point for the mean IR BT radial profiles in Fig. 2, stratified by intensity. Pairings given as (r, BT). Net change represents the change in r and BT from TS to MT intensity. The greatest net change in each variable is highlighted in boldface.

Intensity	L45	FOT	U45	CCT
All	(4.45, 225.5)	(15.2, 217.8)	(28.9, 209.8)	(51.2, 206.6)
TS	(4.45, 207.6)	(13.1, 207.2)	(11.1, 207.2)	(15.6, 207.2)
TY	(4.45, 215.0)	(13.7, 212.7)	(28.9, 209.4)	(49.0, 208.3)
MT	(4.45, 249.1)	(18.4, 225.4)	(31.2, 209.5)	(60.1, 201.4)
Net change	(0, **41.5**)	(5.3, 18.2)	(20.1, 2.3)	(**44.5**, −5.8)

with an IR BT of 225.5 K (Table 3). This warm brightness temperature makes intuitive sense, since cloud tops at the lower extent of the inner eyewall are located lower in the atmosphere than both the cloud tops at the upper extent of the inner eyewall and the coldest cloud tops in the TC inner core. The first overshooting top (FOT; light blue square in Fig. 2a) was located 15.2 km from the TC center in the mean radial profile, with an IR BT of 217.8 K (Table 3). The presence of an overshooting top along the inner eyewall between L45 and U45 in the mean of the 2405 radial profiles indicates the prevalence of deep convection within the inner eyewall region. The upper extent of the inner eyewall (U45, light purple square in Fig. 2a) was located 28.9 km from the TC center in the mean profile with an IR BT of 209.8 K. In addition to being the coldest point (by definition), the CCT was also the most radially outward of the four critical points in the mean profile, with a radial extent of 51.2 km from the TC center and an IR BT of 206.6 K.

The full set of IR BT profiles was then divided into subgroups to investigate the evolution of the mean profiles with increasing intensity. Mean BT profiles were constructed from 588 TS (34–63 kt), 951 TY (64–99 kt), and 866 MT (≥100 kt) profiles (Fig. 1b and gray lines in Figs. 2b–d), and critical points for each of these three mean profiles were determined. Analysis of the mean profiles of the three intensity subcategories (solid black lines, Figs. 2b–d) revealed changes in TC structure with intensity. Inner-core cloud-top IR BTs were nearly uniform in TCs of TS intensity (Fig. 2b). However, as wind speed increased above the TY threshold (Fig. 2c), greater variation in BTs was noted, particularly near the TC center where higher (warmer) brightness temperatures were present. The mean MT profile (Fig. 2d) exhibited even greater variation, with a more vertical profile sloping outward from the TC center, similar to the eyewall profiles in radar reflectivity data reported in previous studies (Corbosiero et al. 2005; Hazelton and Hart 2013). The increasingly vertical slope of the mean profiles with increasing TC intensity is consistent with physical understanding of the development of an eye in more intense TCs (Vigh et al. 2012). It is important to note that the L45 critical point for every mean profile was located at 4.45 km for a nonphysical reason: in each of the mean profiles, the slope of the normalized IR BT profile exceeded 45° at the first point radially outward from the TC center. In individual profiles, the L45 critical point exhibited more variability, which will be discussed in section 3b.

Analysis of the critical points along the mean IR BT radial profiles from the three intensity subgroups (Figs. 2b–d and Table 3) provided additional insight into the evolution of cloud-top structure with intensity. The lower eyewall critical point (L45) remained very close to the TC center at all intensities, revealing that the first upturn (based on the nondimensionalized mean profile) took place within 5 km of the TC center at increasing (warmer) IR BTs, indicative of eye development with increasing intensity. The FOT was located between the lower (L45) and upper (U45) eyewall critical points for the TY and MT mean profiles, indicating that the first tropopause-penetrating convection was within the TC inner eyewall at and above typhoon intensities. For the flatter TS mean profile, this was not the case. The FOT was located radially outward from the L45–U45 inner eyewall segment in the nondimensionalized IR BT radial profile. Interestingly, the FOT exhibited little radial movement between the three intensity subcategories, progressing outward only 5.3 km, yet the associated IR BTs increased substantially, warming 18.2 K. Increasing IR BTs at the near-constant FOT radial location makes physical sense, as the height of the tropopause is lower above the eye than over the surrounding eyewall and inner-core region in mature TCs (Vergados et al. 2014). This enables convection near the TC center to penetrate the tropopause at successively lower heights in the atmosphere (corresponding to successively higher IR BTs) as the eye develops with increasing TC intensity. The U45 critical point exhibited the inverse of the FOT pattern, exhibiting greater radial movement (20.1 km outward) and little change in BT (2.3 K increase) between the mean TS and mean MT profiles. This outward shift of the U45 critical point paralleled the outward radial movement of the CCT critical point. Though the minimum IR BT (CCT) did decrease slightly (cooling 5.8 K) between the mean TS and mean MT profiles, the greatest change for the CCT point was the 44.5-km outward shift in radial location. Within the TS, TY, and MT intensity categories, the greatest variation in critical points was exhibited by this 40+ km radial outward shift of CCT and the 40+ K increase (warming) of L45, which follows a conceptual understanding of a strengthening eyewall (Merrill 1984) and the development of an eye

TABLE 4. Radial distance (r) from the TC center (in km) and IR BT (K) of the mean critical points for each of the six 20-kt intensity bins. Pairings given as (r, BT). Net change represents the change in r and BT from the minimum TS (35–54 kt) to the maximum MT (135+ kt) intensity. The greatest net change in each variable is highlighted in boldface.

Intensity	L45	FOT	U45	CCT
(a) 35–54 kt	(7.2, 220.1)	(12.2, 204.2)	(36.5, 209.3)	(26.0, 202.0)
(b) 55–74 kt	(9.0, 225.3)	(14.0, 206.1)	(46.0, 208.5)	(31.9, 201.1)
(c) 75–94 kt	(8.4, 224.2)	(12.2, 206.9)	(43.0, 205.2)	(44.7, 199.8)
(d) 95–114 kt	(7.0, 237.9)	(14.9, 214.0)	(35.6, 207.3)	(55.3, 201.7)
(e) 115–134 kt	(7.2, 252.5)	(19.7, 217.2)	(29.6, 206.1)	(60.3, 198.3)
(f) 135+ kt	(9.6, 267.5)	(20.8, 218.0)	(31.1, 203.4)	(64.0, 194.8)
Net change	(2.4, **47.4**)	(8.6, 13.8)	(−5.8, 5.9)	(**38.0**, −7.2)

with increasing TC intensity (Vigh et al. 2012). Notably here, the outward radial motion in CCT was greatest (33.4 of 44.5 km or 75%) between TS and TY intensities, and the increase in L45 IR BT was greatest (34.1 of 41.5 K or 82%) between TY and MT intensities.

b. *Changes in critical points with intensity*

To investigate whether the critical point trends found in the mean profiles held for the individual profiles, the 2405 satellite observations were regrouped into 20-kt intensity bins, resulting in six intensity subgroups instead of three (Fig. 1b). Then, in contrast to determining critical points for a single mean profile for each of the three intensity subgroups, critical points for the six subgroups were calculated by averaging the critical point values from the individual profiles within each subgroup (Table 4 and Fig. 5). This was first done for profiles in which all four critical points were present (Fig. 5a), and was then completed for profiles with any critical point present (Fig. 5b). Examination of the mean critical points within each of the smaller intensity bins provided the opportunity to examine the evolution of the TC structural characteristics associated with each critical point in greater detail.

The distribution of the mean critical points that were calculated from the all-critical-point profiles (Fig. 5a) confirmed many of the trends detected in the mean profiles, most notably that the critical points fell into distinct regions along the IR cloud top. Like the pattern in the mean profiles, the L45 point (lower extent of the inner eyewall) was closest to the TC center (at radii less than 10 km) with IR BTs that increased by more than 40 K (primarily while at and above typhoon intensity). The FOT points were tightly grouped near 20 km and 210 K, again indicating the prevalence of tropopause-penetrating convection within the TC inner eyewall. Continuing outward, the mean U45 points that marked the upper extent of the inner eyewall were again at slightly lower (cooler) IR BTs than the mean FOT locations. Unlike the pattern in the mean profiles, however, the near 20-km shift in the radial location of the mean U45 based on the individual profiles was oriented inward rather than outward, a characteristic that can be attributed to the absence of cases in which CCT was located at the TC center. Also unlike the trend noted in the mean profiles, the mean CCT calculated from the individual profiles spanned a much smaller range of radial distances from the TC center, likely due to the exclusion of 354 cases from the mean radial distance calculation where $r_{CCT} = 0$ km.

To investigate the utility of a real-time application in which all available critical points are included in the analysis, a second progression of critical points was examined (Fig. 5b). This meant that an additional 717 CCT, 675 FOT, 20 L45, and 19 U45 critical points, respectively, were included in the calculations of mean critical points across the six 20-kt intensity bins. The general cloud-top structure outlined by these mean critical points (Fig. 5b) was very similar to that observed in the profile-limited cases (Fig. 5a). The 40+ K increase in (warming of) the mean L45 critical point near 10 km from the TC center remained a dominant feature. Furthermore, the mean FOT critical point remained within the inner eyewall, between 10 and 20 km from the TC center, and exhibited a slightly wider range of BTs, extending to colder BTs at weaker intensities (a result of the inclusion of nearly 200 additional cases in each of the lowest two intensity categories). Like the mean L45 positions, the locations of the mean U45 points varied little by easing the four-critical-point constraint. Significant adjustment, however, was noted in the radial locations of the mean CCTs, which were shifted radially inward toward the TC center at lower intensities, a shift that can be explained by the inclusion of CCT points at the center of the TC. This near 40-km-outward movement of the CCT critical point aligned with that observed in the mean IR BT profiles and indicates that monitoring the mean of all critical points in real time potentially may add a new dimension to the current IR BT intensity estimation techniques.

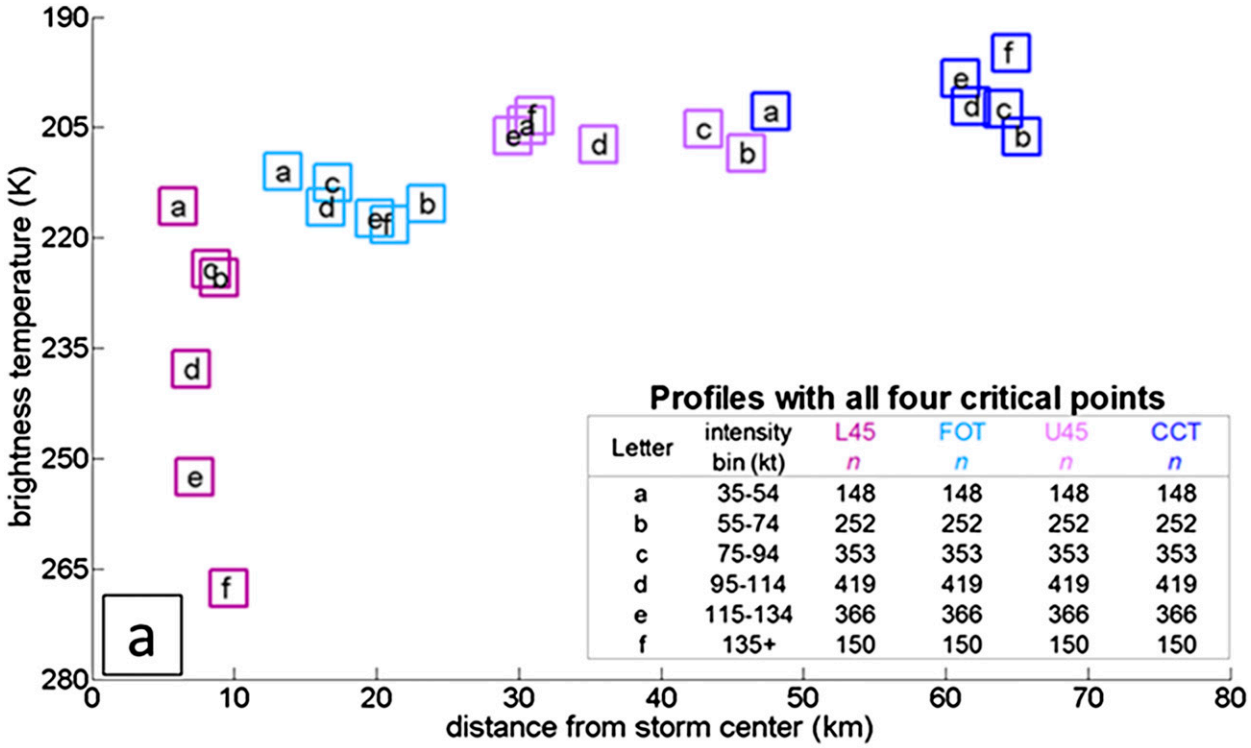

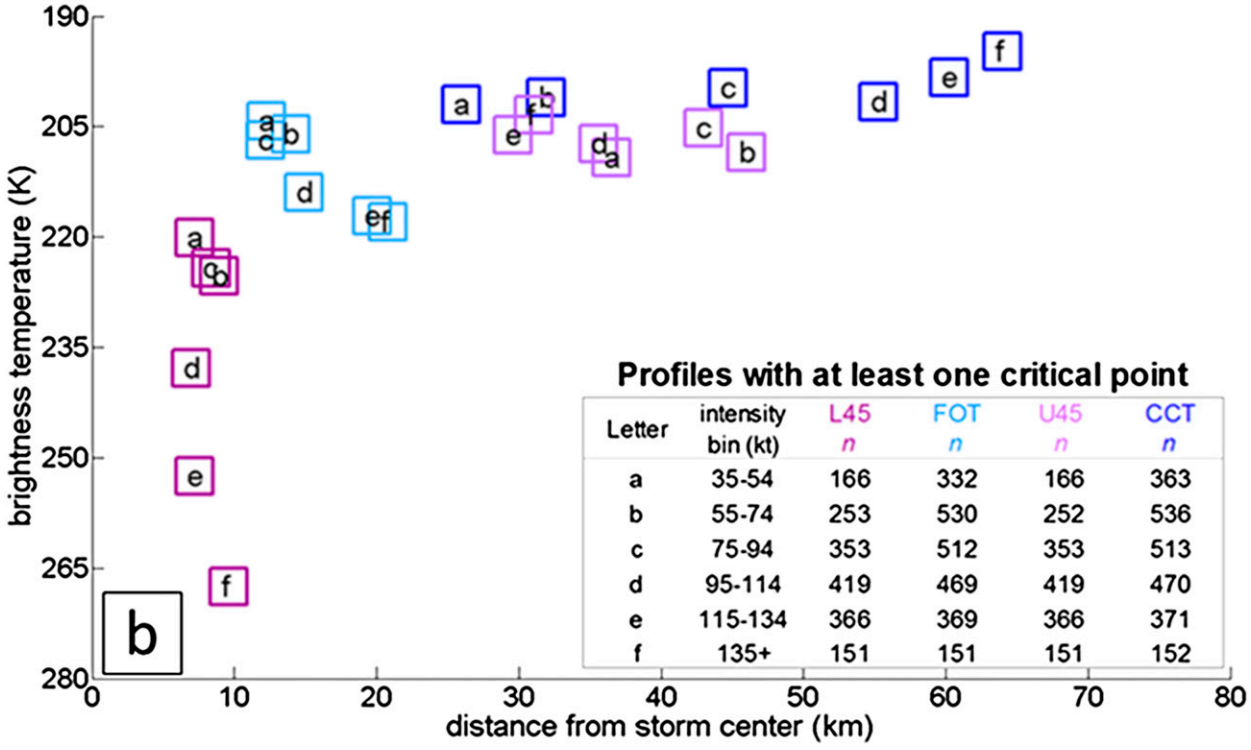

FIG. 5. (a),(b) Mean radial positions (km) and IR BTs (K) of L45 (magenta squares), FOT (light blue squares), U45 (light purple squares), and CCT (blue squares) critical points, stratified by TC intensity (legend letters a–f). Mean critical point calculations in (a) were constrained to profiles in which all four critical points were present, while in (b) every available critical point was included. For each intensity bin, the range (kt) and number (*n*) of radial profiles containing each critical point are listed in the inset table. Values for each radial distance and IR BT for (b) are listed in Table 4.

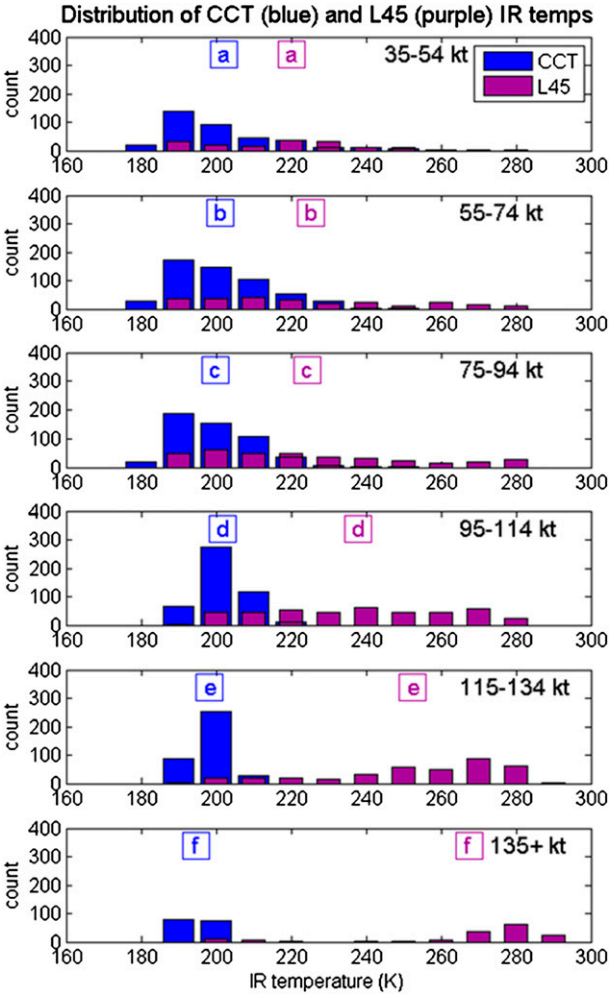

FIG. 6. Counts of IR BTs from every available L45 (magenta) and CCT (blue) critical point for each of the six 20-kt intensity bins. (Totals for each bin match the Fig. 5b inset values.) Boxed letters at the top of each panel indicate the mean IR BT of the L45 and CCT critical points within that bin. Letters a–f correspond to the same intensity categories as in Fig. 5b.

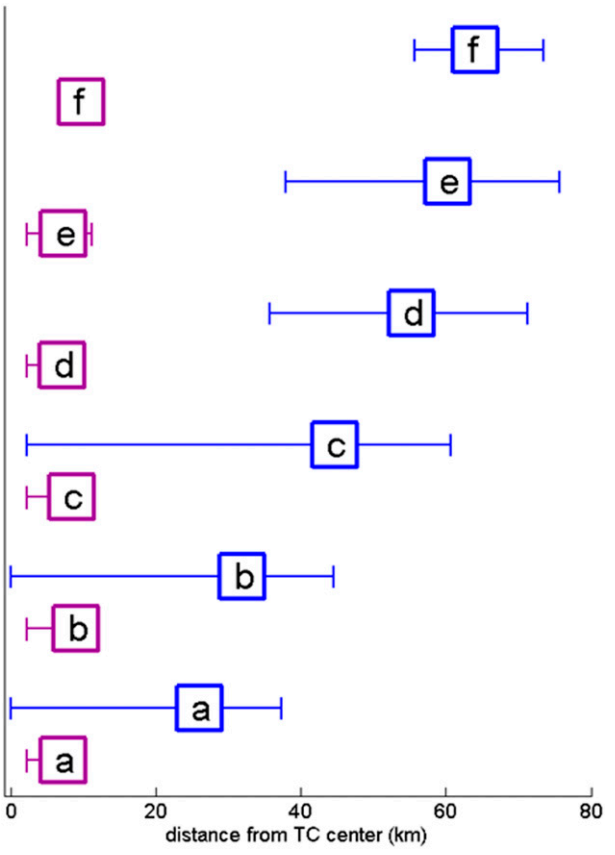

FIG. 7. Variability of radial distance (km) from TC center of CCT (blue boxes) and L45 (purple boxes) for each of the six 20-kt intensity categories in Fig. 5b. Centers of each box represent mean values and left and right whiskers represent 25th and 75th percentile values, respectively. Intensity categories where whiskers are not visible indicate very small ranges of variability (where the whisker is hidden beneath the box).

c. *Critical point variability*

When including all available critical points (Fig. 5b), the greatest change with intensity (i.e., *between* the six 20-kt intensity bins) was found in the increasing IR BT of the mean lower extent of the inner eyewall (L45) and the increasingly outward radial location of the mean CCT. This variability is further illustrated *within* each of the six 20-kt intensity bins (Figs. 6 and 7). While the CCT IR BTs remained clustered near 200 K (blue bars in Fig. 6) within each category, there was a relatively wide range of L45 IR BTs, and the general distribution (and therefore the mean) shifted toward higher IR BTs with increasing intensity. This broad range of L45 IR BTs within each bin will be examined further in the discussion of stratification by latitude. The CCT demonstrated greater variability than L45 in radial distance from the TC center (Fig. 7) and was most notable radially inward from the mean in the lowest three 20-kt intensity bins (boxed blue letters a–c with associated whiskers in Fig. 7). These three intensity bins had the highest percentages of center-CCT and non-eyewall cases (Figs. 5a,b), which contributed toward the outward progression of the mean CCT critical point with increasing intensity.

Stratifying the critical point cases by latitude (Figs. 8a,b) and vertical wind shear (Figs. 8c,d) provided further insight into the structural changes in the inner core as the TC intensity changed. With regard to IR BT, stratification by latitude yielded apparently contrasting results. At lower latitudes, the L45 point spanned a 60-K range in IR BT, while the CCT IR BT remained nearly constant around 195 K. Conversely, at higher latitudes,

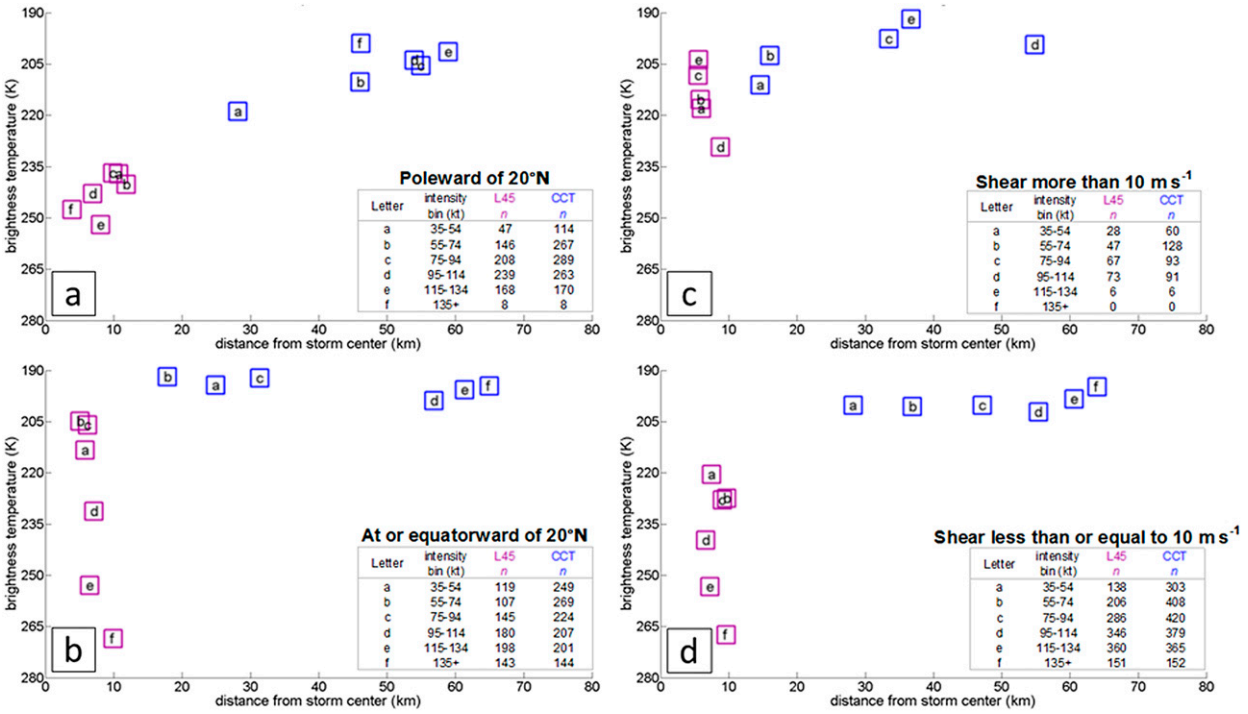

FIG. 8. As in Fig. 5b, but only for L45 and CCT critical points stratified by (left) latitude and (right) 850–200-hPa vertical wind shear. Latitude stratification based on TC center location (a) poleward and (b) at and equatorward of 20°N. Shear stratification based on 850–200-hPa vertical wind shear of (c) > and (d) $\leq 10\,\mathrm{m\,s^{-1}}$.

the L45 range of IR BTs was much smaller (<20 K), while the CCT IR BTs varied by more than 20 K. Since most TCs included in this analysis formed (decayed) south (north) of 20°N, these results could imply that warming of the lower extent of the inner eyewall (i.e., eye development) is prevalent during intensification, and that during decay cloud tops warm as convection weakens in the TC inner core. It was also noted that relatively higher (lower) IR BTs were present in the lower- (higher-) latitude cases, which is likely related to differences in tropopause height with latitude.

The radial location of the mean CCT exhibited a clear relationship to latitude. The outward progression of the mean CCT with increasing intensity at both higher and lower latitudes (Figs. 8a,b) was similar to that observed in the progression of the mean CCTs calculated from every available critical point (Fig. 5b). In the full dataset, however, the greatest outward radial movement spanned 23.4 km (Table 4) and was relatively evenly distributed between intensity bins b and d. In the latitude subsets, the outward progression occurred at different intensities. At higher latitudes, the greatest outward radial movement occurred between intensity bins a and b, while at lower latitudes, the greatest outward motion occurred between intensity bins c and d. These differences in radial location of the mean CCT are hypothesized to depend on the prevalence of CDO-like conditions at different intensities (i.e., where the CCT location at the TC center would reduce the mean CCT radial location among the profiles for the affected intensity bin). Coupled with the difference in IR BTs with latitude noted above, this difference in the outward progression of the mean coldest cloud tops may indicate that tropopause height impacts eye development; that is, cold cloud tops clear the eye and deep convection moves radially outward at lower intensities and warmer BTs at higher latitudes where the tropopause is lower in the atmosphere.

Dividing the 2405 cases by vertical wind shear (Figs. 8c,d) revealed that low-shear conditions (vertical wind shear less than or equal to $10\,\mathrm{m\,s^{-1}}$) were the most prevalent, composing 84.3% of CCT cases and 87.1% of L45 cases (Figs. 4c,d). In these conditions, the patterns in both CCT and L45 were very close to those exhibited in the full dataset (outward movement of the mean CCT and increasing IR BT of the mean L45 with intensity). While the high-shear cases composed only a small percentage of the overall dataset, the trend of radially outward movement of the mean CCT point remained prevalent. In contrast to previous results, however, the general tendency of the L45 BT was to decrease (rather than to increase) with intensity. The mean L45 points were also generally much warmer in the high-shear cases

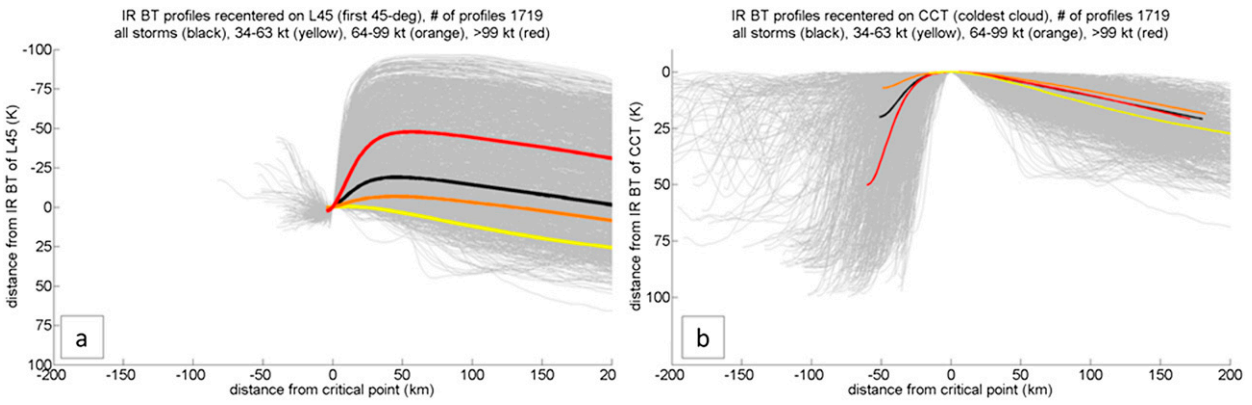

FIG. 9. Individual (light gray lines) and mean (dark colored lines) IR BT profiles, recentered on (a) the L45 critical point and (b) the CCT critical point. Mean profiles are highlighted for all TC intensities (black lines), TC intensities 34–63 kt (yellow lines), TC intensities 64–99 kt (orange lines), and TC intensities ≥ 100 kt (red lines).

than in the low-shear cases, which would indicate that the lower extent of the inner eyewall was located higher in the atmosphere in high-shear cases. This cooling with intensity and higher eyewall-base height are difficult to interpret due to the multiple ways in which a vortex may respond to shear (Davis et al. 2008) and due to the challenges of identifying the TC center in high-shear cases.

d. Cloud-top slope

Upon inspection, it was clear that the shapes of the mean radial IR BT profiles changed with intensity (Figs. 2b–d). More precisely, the inner-core IR BT profile in the eyewall became more vertical with increasing intensity, which gave it a more negative slope. Recentering these mean profiles at the radial locations and brightness temperatures of L45 (Fig. 9a) and CCT (Fig. 9b) highlights the qualitative differences between the four profiles. When centered at the L45 radius, the mean TS profile (in yellow) showed very little vertical variation, moving radially outward (Fig. 9a) from the L45 location. A slight increase in BT was noted in the TY profile (in orange) to the right of L45. A steeper slope was noted in the mean of all the profiles (in black), and the steepest of slopes corresponded to the mean MT profile (in red). A similar effect was noted when the profiles were recentered at the radial location and BT of the CCT. However, the sloped profiles extended inward from that point (Fig. 9b) instead of outward. These mean profiles highlight that the slope of the IR BT profile changed with intensity; specifically, the BT profiles became more vertical in the inner eyewall region with increasing intensities.

To quantitatively assess relationships between the slopes and intensities of the 2405 radial profiles, six slopes of IR BT were calculated for each profile, each based on a segment between two critical points: L45 and U45, L45 and FOT, L45 and CCT, FOT and U45, U45 and CCT, and FOT and CCT (Figs. 3, 10, and 11, and Table 5). Statistically significant (at the 95% confidence level) negative correlations were found between the current slope of the inner-core cloud-top IR BTs and the current TC intensity (Table 5, row 1a; all correlations statistically significant at the 95% confidence level are noted in boldface in Table 5). A negative correlation between slope and intensity indicated that stronger TCs had more negative slopes, and a negative slope indicated that IR BT decreased outward from the TC center. The strongest relationship (−0.663 correlation) appeared in the inner eyewall between the L45 and U45 slope and intensity (Table 5, row 1a and Fig. 10a), which is consistent with the progression of radius and IR BT of L45 and U45 critical points with intensity (Table 4). Similar statistically significant negative correlations were found for the L45–FOT and FOT–U45 segments of the inner eyewall. As the slope of the lines connecting these critical points decreased (i.e., the inner eyewall BT profile became more vertical), the intensity of the TC increased. This relationship between current slope and current intensity extended to all six critical point segments, where correlations ranged between −0.426 and −0.663, with a mean correlation of −0.581. Similar correlations between L45 and U45 slope and intensity were also found for each *individual* storm, albeit with somewhat more variability, with correlation coefficients ranging from −0.373 to −0.798 for the 11 TCs with more than 30 satellite observations where slopes were calculable.

In addition to correlating the current slope with the current intensity, *changes* in slope were correlated to *changes* in intensity. Significant negative correlations were found between changes in slope over a 24-h period and changes in intensity over the same 24-h period, suggesting that within a 24-h period, decreases in eyewall slope (profile becoming more vertical) were related to

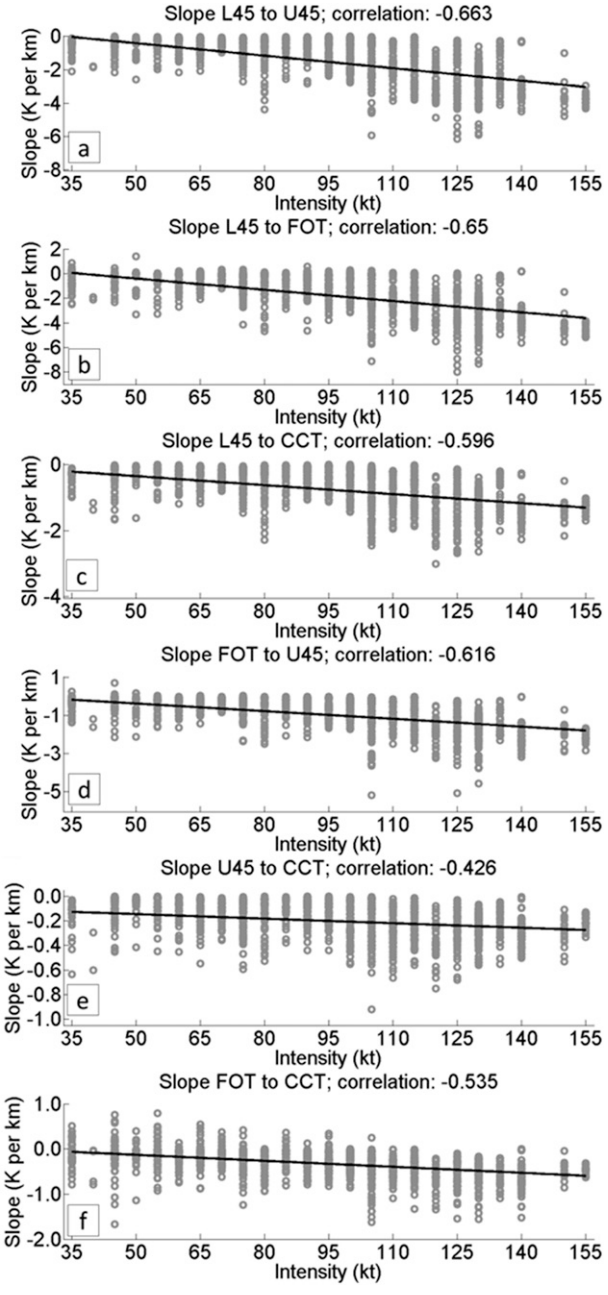

FIG. 10. Slope (K km^{-1}) vs intensity (kt) for (a) L45–U45, (b) L45–FOT, (c) L45–CCT, (d) FOT–U45, (e) U45–CCT, and (f) FOT–CCT. Black line in each panel indicates linear regression of slope from 35 to 155 kt.

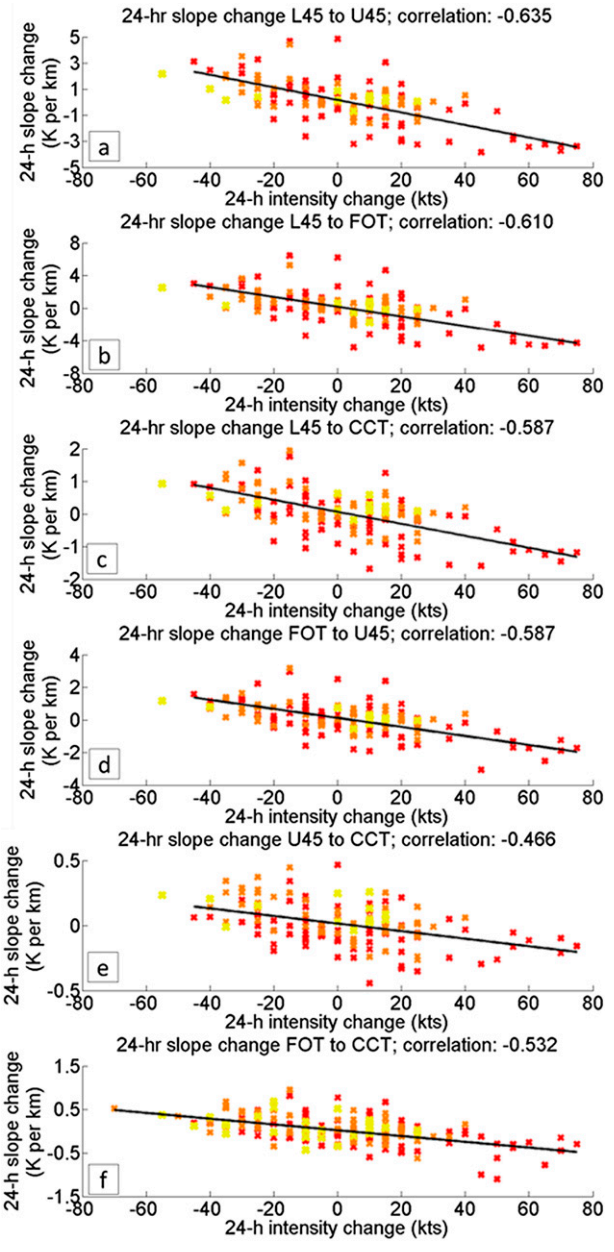

FIG. 11. As in Fig. 10, but for 24-h change in slope (K km^{-1}) vs 24-h change in intensity (kt). Colored markers represent the intensity of the TC at the start of the 24-h period, i.e., yellow markers for starting intensities 34–63 kt, orange markers for starting intensities 64–99 kt, and red markers for starting intensities ≥ 100 kt.

increases in intensity [and that increases in eyewall slope (profile becoming more flat) were related to decreases in intensity]. The strongest relationship (−0.635 correlation; Table 5, row 2a; Fig. 11a) again appeared in the slope of the segment between the lower and upper extents of the inner eyewall (L45–U45) and intensity, indicating that within a 24-h period, the slope between those two points decreased (increased) as the TC intensified (weakened). This relationship was found to hold regardless of TC intensity, as seen by the similar pattern of scatter in the TS (yellow), TY (orange), and MT (red) points in Fig. 11a.

A final set of correlations was used to examine possible lead–lag relationships between slope and intensity. Slope changes over a 12-h period were found to be statistically

TABLE 5. Pearson product-moment correlation coefficients between current slope and current intensity (row 1), 24-h change in slope with 24-h change in intensity (row 2), 12-h change in slope followed by 12-h change in intensity (row 3), and 12-h change in intensity followed by 12-h change in slope (row 4). Boldface text denotes statistically significant correlations at the 95% confidence level.

	L45–U45	L45–FOT	L45–CCT	FOT–U45	U45–CCT	FOT–CCT	Mean
1) Correlation of current slope to current intensity							
(a) All storms	**−0.663**	**−0.650**	**−0.596**	**−0.616**	**−0.426**	**−0.535**	−0.581
(b) Lat ≤ 20°N	**−0.682**	**−0.658**	**−0.633**	**−0.613**	**−0.469**	**−0.508**	−0.594
(c) Lat > 20°N	**−0.608**	**−0.618**	**−0.534**	**−0.613**	**−0.415**	**−0.585**	−0.562
(d) Shear ≤ 10 m s^{-1}	**−0.665**	**−0.653**	**−0.592**	**−0.613**	**−0.413**	**−0.516**	−0.575
(e) Shear > 10 m s^{-1}	**−0.409**	**−0.359**	**−0.406**	**−0.417**	**−0.364**	**−0.549**	−0.417
2) Correlation of 24-h slope change to 24-h intensity change, over the same period							
(a) All storms	**−0.635**	**−0.610**	**−0.587**	**−0.587**	**−0.466**	**−0.532**	−0.569
(b) Lat ≤ 20°N	**−0.626**	**−0.579**	**−0.593**	**−0.582**	**−0.425**	**−0.557**	−0.560
(c) Lat > 20°N	**−0.641**	**−0.672**	**−0.578**	**−0.593**	**−0.505**	**−0.465**	−0.576
(d) Shear ≤ 10 m s^{-1}	**−0.665**	**−0.638**	**−0.601**	**−0.604**	**−0.457**	**−0.538**	−0.584
(e) Shear > 10 m s^{-1}	−0.363	−0.345	−0.395	−0.375	−0.384	**−0.483**	−0.391
3) Correlation of 12-h slope change to intensity change over the next 12 h							
(a) All storms	**−0.292**	**−0.348**	**−0.278**	**−0.363**	**−0.348**	**−0.359**	−0.331
(b) Lat ≤ 20°N	−0.173	−0.208	−0.074	**−0.250**	−0.227	−0.221	−0.192
(c) Lat > 20°N	**−0.341**	**−0.433**	**−0.423**	**−0.433**	**−0.430**	**−0.439**	−0.416
(d) Shear ≤ 10 m s^{-1}	**−0.290**	**−0.322**	**−0.248**	**−0.339**	**−0.328**	**−0.329**	−0.309
(e) Shear > 10 m s^{-1}	−0.284	−0.363	−0.294	−0.341	−0.276	−0.385	−0.324
4) Correlation of 12-h intensity change to slope change over the next 12 h							
(a) All storms	0.050	0.096	0.109	0.071	0.099	0.086	0.085
(b) Lat ≤ 20°N	0.160	0.165	0.190	0.112	0.122	0.127	0.146
(c) Lat > 20°N	0.016	0.023	0.045	0.027	0.078	0.046	0.039
(d) Shear ≤ 10 m s^{-1}	0.072	0.112	0.135	0.085	0.113	0.101	0.103
(e) Shear > 10 m s^{-1}	−0.395	−0.372	−0.533	−0.586	−0.423	−0.372	−0.447

significantly negatively correlated to intensity changes over the following 12-h period (Table 5, row 3a), but intensity changes over a 12-h period were found to have no relationship to changes in slope over the following 12-h period (Table 5, row 4a). Correlations for all six eyewall segments were also statistically significant at the 95% confidence level, ranging from −0.292 to −0.363 with a mean of −0.331, indicating that decreases (increases) in the slope of the eyewall over a 12-h period were followed in the next 12-h period by increases (decreases) in TC intensity. Physically, this can be extended to mean that structure change leads intensity change, and also that changes in the secondary circulation lead changes in the primary circulation.

Stratifying the 2405 cases by latitude revealed that correlations of current slope to current intensity (Table 5, rows 1b,c) and previous 24-h slope change to previous 24-h intensity change (Table 5, rows 2b,c) for both latitude bands generally remained consistent with the results for all storms and for previous radar-based eyewall studies. That is, statistically significant negative correlations were present, indicating higher- (lower-) intensity storms would have a more (less) vertically oriented eyewall, and particularly so for the lower eyewall segments at higher latitudes. Given the outward radial motion of CCT (over both latitude bands) and the increase in L45 IR BTs (at lower latitudes) and decrease in CCT IR BTs (at higher latitudes) discussed in the previous section, the similarity of these correlations for both latitude bands was somewhat expected.

The lead–lag results, however, revealed differences for the lower- and higher-latitude cases, corroborating the all-storms analysis. With statistically significant correlations of 12-h slope change to subsequent 12-h intensity change (Table 5, row 3c), and near-zero (and statistically insignificant) correlations of 12-h intensity change to subsequent 12-h slope change (Table 5, row 4c), it was evident that at higher latitudes, changes in eyewall slope were much more apt to lead (rather than to lag) changes in TC intensity. This differed from the lower-latitude cases, in which correlations for both the lead and lag scenarios (Table 5, rows 3b and 4b) were generally weak. In fact, for the case of slope change leading intensity change (Table 5, rows 3b,c), higher-latitude correlations nearly doubled the values found in lower-latitude cases across every eyewall segment, meaning that changes in eyewall slope (secondary circulation) were almost twice as likely to lead changes in TC intensity (primary circulation) at higher latitudes than at lower latitudes. One physical reason for the stronger relationship and increased correlations at higher latitudes may be traced to the impact of the tropopause. Since at higher latitudes there is less space for the vertical development of deep convection and the outward radial movement of the CCT takes place at

lower intensities, perhaps the lower tropopause height enhances the coupling between the secondary and primary circulations. Likewise, since there is greater space for vertical development of deep convection at lower latitudes and the outward radial movement of the CCT is observed at higher intensities, perhaps the higher tropopause height somewhat weakens the connection between the secondary and primary TC circulations.

Low-shear cases followed the patterns described previously for current slope and current intensity (Table 5, row 1d), 24-h slope change and 24-h intensity change (Table 5, row 2d), and lead–lag relationships (Table 5, rows 3d and 4d): strongest correlations were in the inner eyewall, weakest correlations were in the upper eyewall; changes in eyewall slope led changes in TC intensity; and all correlations (except the lagged correlations) for low-shear cases were statistically significant at the 95% confidence level. For the small percentage of highly sheared systems, however, the results were different, in that the most negative correlations were found in the mid- to upper eyewall segment (Table 5, rows 1e and 2e), and changes in TC intensity led changes in TC slope in the middle and total eyewall segments (although none of the lead or lag correlations were statistically significant, due to the small sample size). While these results suggest that vertically sheared systems lose structural coherence prior to decaying in intensity, because the high-shear cases composed a relatively small percentage of the full dataset, further analysis of change in eyewall slope in highly sheared cases is recommended.

4. Discussion and conclusions

Cloud-top brightness temperatures have long been associated with the intensity of the surface wind field in a tropical cyclone. In this study, 2405 satellite observations spanning 14 TCs from the 2012 western North Pacific TC season were used to accomplish two objectives: 1) examine properties of four critical points in satellite-derived radial profiles of IR BT and analyze variations with intensity and 2) relate both current slope of IR BT with current intensity and changes in slope of IR BT with changes in intensity. Variation in BT of the coldest cloud top (CCT) with TC intensity was found to be relatively small, while much greater variation was noted in the IR BT of L45, the lower extent of the inner eyewall, which warmed significantly between tropical storm and the strongest typhoon intensities, particularly in lower latitudes. Radial movement of the coldest cloud top was relatively large as the TC changed intensity, and the mean CCT was located farther from the center in stronger TCs. Physically, this can be interpreted to mean that between TS and TY intensities, the TC eye develops and is cleared of cold cloud tops, and that between TY and MT intensities, the eye deepens as the eyewall increases in vertical extent. Future work is planned to use these results to improve current intensity estimation techniques that consider IR brightness temperatures in the inner core.

Traditionally, very cold cloud tops have been associated with deep convection and regions of strong upward vertical motion. In TCs they often represent the ''up'' branch of the ''in–up–out'' secondary circulation pattern. Further, colder cloud tops (stronger secondary circulation) have also been associated with more intense storms (stronger primary circulation) (Shapiro and Willoughby 1982; Willoughby et al. 1982). It is considered noteworthy here that, perhaps in contrast to previous cases, the IR brightness temperature of the coldest cloud top varied little, while the lower extent of the TC inner eyewall IR BT increased substantially. As a result, stronger TCs did exhibit greater differences in IR BT between L45 and CCT, and these differences are related to current operational TC intensity estimation techniques. For example, the difference in IR BT between L45 and CCT is similar to aspects of the Dvorak technique, in that the greater the difference between these BTs, the more intense the storm. However, not captured in the Dvorak technique is the significance of the radially outward progression of the mean coldest cloud top, and the resulting similar relationship in the radial separation of these two critical points, namely that the greatest separation occurs during the periods of greatest intensity. This outward radial movement in CCT coupled with the increase in L45 IR BT foreshadowed the relationship between eyewall slope and TC intensity.

The primary conclusions from the slope analysis were as follows. First, the current slope of IR BT was negatively correlated to the current TC intensity in every segment of the TC inner core, meaning that stronger (weaker) TCs had more (less) negative slopes of IR BT and more (less) vertical eyewall profiles. The strongest negative correlation was found in the inner eyewall (L45–U45) region of the TC inner core. Of the two segments composing the inner eyewall (L45–FOT and FOT–U45), a stronger correlation was found in the lower eyewall (L45–FOT), which is consistent with earlier studies of eyewall slope that were based on limited high-resolution reconnaissance aircraft radar measurements (Corbosiero et al. 2005; Hazelton and Hart 2013). Second, except in high-shear cases, changes in slope over a 24-h period were strongly negatively

correlated to changes in intensity over the same 24-h period, revealing a link between slope change and intensity change. Once again, the strongest correlation was found in the inner eyewall (L45–U45) and the lowest portion of the eyewall (L45–FOT) had the stronger correlation of the two inner eyewall segments. Finally, also with the exception of high-shear cases, the relationship between change in slope and change in intensity appears to support a lead, versus a lag, relationship, whereby changes in slope lead changes in intensity, particularly for higher-latitude cases. This result lends credence to the argument that changes in the TC secondary circulation (cloud updrafts) lead changes in the primary circulation (tangential surface winds) for both strengthening and weakening TCs.

Although the results in this study were based on 2405 cases and appeared consistently across 14 TCs, it is important to note several factors. First, the JTWC TC intensities used for the study were likely based, at least in part, on results from the satellite-driven Dvorak technique. However, the operational Dvorak technique does not explicitly take into account radial gradients like those computed in this study, giving confidence to the robustness of the slope–intensity relationships found here. Second, the 14 TCs analyzed included only those that reached TY intensity. However, 588 of the 2405 satellite observations were made when the TC was at TS intensity, and critical point movement and slope calculations from those weaker storms proved important to the overall results of the study. Third, all available TC profiles were analyzed in this study, including those that may have had asymmetric brightness temperatures, those with possible land interaction, or those with concentric eyewalls. The consideration of a variety of IR BT profiles in the analysis gives additional confidence to the applicability of the results reported here.

Acknowledgments. The authors thank Jeffrey Hawkins, Kim Richardson, and the entire satellite group at the Naval Research Laboratory-Monterey for providing processed *MTSAT-2* satellite data for the 2012 western North Pacific season. The authors also thank Mark DeMaria for his assistance with the shear criteria in the SHIPS developmental data. The authors are also grateful for the efforts of Cassandra Merino and Anna Haschert, who were funded by the American Society for Engineering Education's (ASEE) Science and Engineering Apprenticeship Program (SEAP), for their assistance in the early stages of the project. Partial support for this study was provided by the Naval Academy Research Council and the Naval Academy Office of Midshipman Research.

REFERENCES

Bankert, R. L., and P. M. Tag, 2002: An automated method to estimate tropical cyclone intensity using SSM/I imagery. *J. Appl. Meteor.,* **41,** 461–472, doi:10.1175/1520-0450(2002)041<0461:AAMTET>2.0.CO;2.

Black, R. A., H. B. Bluestein, and M. L. Black, 1994: Unusually strong vertical motions in a Caribbean hurricane. *Mon. Wea. Rev.,* **122,** 2722–2739, doi:10.1175/1520-0493(1994)122<2722:USVMIA>2.0.CO;2.

Brown, D. P., and J. L. Franklin, 2004: Dvorak tropical cyclone wind speed biases determined from reconnaissance-based "best track" data (1997–2003). *26th Conf. on Hurricanes and Tropical Meteorology,* Miami, FL, Amer. Meteor. Soc., 3D.5. [Available online at http://ams.confex.com/ams/pdfpapers/75193.pdf.]

Chu, J.-H., C. R. Sampson, A. S. Levine, and E. Fukada, 2002: The Joint Typhoon Warning Center tropical cyclone best-tracks, 1945-2000. Naval Research Laboratory Ref. NRL/MR/7540-02-16, 112 pp.

Corbosiero, K. L., and J. Molinari, 2002: The effects of vertical wind shear on the distribution of convection in tropical cyclones. *Mon. Wea. Rev.,* **130,** 2110–2123, doi:10.1175/1520-0493(2002)130<2110:TEOVWS>2.0.CO;2.

——, ——, and M. L. Black, 2005: The structure and intensification of Hurricane Elena (1985). Part I: Symmetric intensification. *Mon. Wea. Rev.,* **133,** 2905–2921, doi:10.1175/MWR3010.1.

Davis, C. A., S. C. Jones, and M. Riemer, 2008: Hurricane vortex dynamics during Atlantic extratropical transition. *J. Atmos. Sci.,* **65,** 714–736, doi:10.1175/2007JAS2488.1.

Dvorak, V. F., 1972: A technique for the analysis and forecasting of tropical cyclone intensities from satellite pictures. NOAA Tech. Memo. NES 36, 15 pp.

——, 1975: Tropical cyclone intensity analysis and forecasting from satellite imagery. *Mon. Wea. Rev.,* **103,** 420–430, doi:10.1175/1520-0493(1975)103<0420:TCIAAF>2.0.CO;2.

——, 1984: Tropical cyclone intensity analysis using satellite data. NOAA Tech. Rep. 11, 45 pp.

——, 1995: *Tropical Clouds and Cloud Systems Observed in Satellite Imagery: Tropical Cyclones.* Workbook Vol. 2, NOAA/NESDIS, 359 pp. [Available from NOAA/NESDIS, 5200 Auth Rd., Washington, DC 20333.]

Eliassen, A., 1951: Slow thermally or frictionally controlled meridional circulation in a circular vortex. *Astrophys. Norv.,* **5,** 19–60.

Erickson, C. O., 1967: Some aspects of the development of Hurricane Dorothy. *Mon. Wea. Rev.,* **95,** 121–130, doi:10.1175/1520-0493(1967)095<0121:SAOTDO>2.3.CO;2.

Fett, R. W., 1964: Aspects of hurricane structure: New model considerations suggested by TIROS and Project Mercury observations. *Mon. Wea. Rev.,* **92,** 43–60, doi:10.1175/1520-0493(1964)092<0043:AOHSNM>2.3.CO;2.

Fritz, S., and I. Laszlo, 1993: Detection of water vapor in the stratosphere over very high clouds in the tropics. *J. Geophys. Res.,* **98,** 22 959–22 967, doi:10.1029/93JD01617.

——, L. F. Hubert, and A. Timchalk, 1966: Some inferences from satellite pictures of tropical disturbances. *Mon. Wea. Rev.,* **94,** 231–236, doi:10.1175/1520-0493(1966)094<0231:SIFSPO>2.3.CO;2.

Hawkins, H. F., and S. M. Imbembo, 1976: The structure of a small, intense Hurricane Inez 1966. *Mon. Wea. Rev.,* **104,** 418–442, doi:10.1175/1520-0493(1976)104<0418:TSOASI>2.0.CO;2.

Hazelton, A. T., and R. E. Hart, 2013: Hurricane eyewall slope as determined from airborne radar reflectivity data: Composites and case studies. *Wea. Forecasting,* **28,** 368–386, doi:10.1175/WAF-D-12-00037.1.

Jorgensen, D. P., 1984: Mesoscale and convective-scale characteristics of mature hurricanes. Part I: General observations by research aircraft. *J. Atmos. Sci.,* **41,** 1268–1286, doi:10.1175/1520-0469(1984)041<1268:MACSCO>2.0.CO;2.

Kossin, J. P., and C. S. Velden, 2004: A pronounced bias in tropical cyclone minimum sea level pressure estimation based on the Dvorak technique. *Mon. Wea. Rev.,* **132,** 165–173, doi:10.1175/1520-0493(2004)132<0165:APBITC>2.0.CO;2.

Maclay, K. S., M. DeMaria, and T. H. Vonder Haar, 2008: Tropical cyclone inner-core kinetic energy evolution. *Mon. Wea. Rev.,* **136,** 4882–4898, doi:10.1175/2008MWR2268.1.

Marks, F. D., 1985: Evolution of the structure of precipitation in Hurricane Allen (1980). *Mon. Wea. Rev.,* **113,** 909–930, doi:10.1175/1520-0493(1985)113<0909:EOTSOP>2.0.CO;2.

Markus, R. M., N. F. Halbeisen, and J. F. Fuller, 1987: Air Weather Service; our heritage, 1937-1987. Military Airlift Command, U.S. Air Force, Scott AFB, IL, 167 pp.

Merrill, R. T., 1984: A comparison of large and small tropical cyclones. *Mon. Wea. Rev.,* **112,** 1408–1418, doi:10.1175/1520-0493(1984)112<1408:ACOLAS>2.0.CO;2.

Olander, T. L., and C. S. Velden, 2007: The advanced Dvorak technique: Continued development of an objective scheme to estimate tropical cyclone intensity using geostationary infrared satellite imagery. *Wea. Forecasting,* **22,** 287–298, doi:10.1175/WAF975.1.

——, and ——, 2009: Tropical cyclone convection and intensity analysis using differenced infrared and water vapor imagery. *Wea. Forecasting,* **24,** 1558–1572, doi:10.1175/2009WAF2222284.1.

Piñeros, M. F., E. A. Ritchie, and J. S. Tyo, 2011: Estimating tropical cyclone intensity from infrared image data. *Wea. Forecasting,* **26,** 690–698, doi:10.1175/WAF-D-10-05062.1.

Raman, M. R., and W.-N. Chen, 2014: Trends in monthly characteristics observed over Taipei, Taiwan. *J. Atmos. Sci.,* **71,** 1323–1338, doi:10.1175/JAS-D-13-0230.1.

Ritchie, E. A., and W. M. Frank, 2007: Interactions between simulated tropical cyclones and an environment with a variable Coriolis parameter. *Mon. Wea. Rev.,* **135,** 1889–1905, doi:10.1175/MWR3359.1.

——, G. Valliere-Kelley, M. F. Piñeros, and J. S. Tyo, 2012: Tropical cyclone intensity estimation in the North Atlantic basin using an improved deviation angle variance technique. *Wea. Forecasting,* **27,** 1264–1277, doi:10.1175/WAF-D-11-00156.1.

Rogers, R., S. Lorsolo, P. Reasor, J. Gamache, and F. Marks, 2012: Multiscale analysis of tropical cyclone kinematic structure from airborne Doppler radar composites. *Mon. Wea. Rev.,* **140,** 77–99, doi:10.1175/MWR-D-10-05075.1.

Sadler, J. C., 1964: Tropical cyclones of the eastern North Pacific as revealed by TIROS observations. *J. Appl. Meteor.,* **3,** 347–366, doi:10.1175/1520-0450(1964)003<0347:TCOTEN>2.0.CO;2.

Schubert, W. H., and B. D. McNoldy, 2010: Application of the concepts of Rossby length and Rossby depth to tropical cyclone dynamics. *J. Adv. Model. Earth Syst.,* **2** (7), doi:10.3894/JAMES.2010.2.7.

Shapiro, L. J., and H. E. Willoughby, 1982: The response of balanced hurricanes to local sources of heat and momentum. *J. Atmos. Sci.,* **39,** 378–394, doi:10.1175/1520-0469(1982)039<0378:TROBHT>2.0.CO;2.

Shea, D. J., and W. M. Gray, 1973: The hurricane's inner core region. I. Symmetric and asymmetric structure. *J. Atmos. Sci.,* **30,** 1544–1564, doi:10.1175/1520-0469(1973)030<1544:THICRI>2.0.CO;2.

Sheets, R. C., 1990: The National Hurricane Center—Past, present, and future. *Wea. Forecasting,* **5,** 185–232, doi:10.1175/1520-0434(1990)005<0185:TNHCPA>2.0.CO;2.

Stern, D. P., and D. S. Nolan, 2009: Reexamining the vertical structure of tangential winds in tropical cyclones: Observations and theory. *J. Atmos. Sci.,* **66,** 3579–3600, doi:10.1175/2009JAS2916.1.

Thuburn, J., and G. C. Craig, 1997: GCM tests of theories for the height of the tropopause. *J. Atmos. Sci.,* **54,** 869–882, doi:10.1175/1520-0469(1997)054<0869:GTOTFT>2.0.CO;2.

Velden, C. S., T. L. Olander, and R. M. Zehr, 1998: Development of an objective scheme to estimate tropical cyclone intensity from digital geostationary satellite infrared imagery. *Wea. Forecasting,* **13,** 172–186, doi:10.1175/1520-0434(1998)013<0172:DOAOST>2.0.CO;2.

——, and Coauthors, 2006: The Dvorak tropical cyclone intensity estimation technique: A satellite-based method that has endured for over 30 years. *Bull. Amer. Meteor. Soc.,* **87,** 1195–1210, doi:10.1175/BAMS-87-9-1195.

Vergados, P., Z. J. Luo, K. Emanuel, and A. J. Mannucci, 2014: Observational tests of hurricane intensity estimations using GPS radio occultations. *J. Geophys. Res. Atmos.,* **119,** 1936–1948, doi:10.1002/2013JD020934.

Vigh, J. L., J. A. Knaff, and W. H. Schubert, 2012: A climatology of hurricane eye formation. *Mon. Wea. Rev.,* **140,** 1405–1426, doi:10.1175/MWR-D-11-00108.1.

Willoughby, H. E., 1979: Forced secondary circulations in hurricanes. *J. Geophys. Res.,* **84,** 3173–3183, doi:10.1029/JC084iC06p03173.

——, J. A. Clos, and M. G. Shoreibah, 1982: Concentric eyewalls, secondary wind maxima, and the evolution of the hurricane vortex. *J. Atmos. Sci.,* **39,** 395–411, doi:10.1175/1520-0469(1982)039<0395:CEWSWM>2.0.CO;2.

Wimmers, A. J., and C. S. Velden, 2010: Objectively determining the rotational center of tropical cyclones in passive microwave satellite imagery. *J. Appl. Meteor. Climatol.,* **49,** 2013–2034, doi:10.1175/2010JAMC2490.1.

Zhao, K., M. Xue, and W.-C. Lee, 2012: Assimilation of GBVTD-retrieved winds from single-Doppler radar for short-term forecasting of super typhoon *Saomai* (0608) at landfall. *Quart. J. Roy. Meteor. Soc.,* **138,** 1055–1071, doi:10.1002/qj.975.